

JGR Space Physics

RESEARCH ARTICLE

10.1029/2020JA028949

Key Points:

- We have built and compared 28 Pedersen conductance maps based on ultraviolet spectrograph spectral images collected during the 15 first Juno orbits
- The mean conductance is 0.47 mho in both hemispheres, a symmetry in contrast with the asymmetry observed in the ionospheric currents
- The auroral H₂ emitted power varies between 1.1 and 3.6 TW but the north/south power ratio is close to unity on the average

Correspondence to:

J.-C. Gérard,
jc.gerard@uliege.be

Citation:

Gérard, J.-C., Gkouvelis, L., Bonfond, B., Grodent, D., Gladstone, G. R., Hue, V., et al. (2021). Variability and hemispheric symmetry of the Pedersen conductance in the Jovian aurora. *Journal of Geophysical Research: Space Physics*, 126, e2020JA028949. <https://doi.org/10.1029/2020JA028949>

Received 19 NOV 2020
Accepted 22 FEB 2021

Variability and Hemispheric Symmetry of the Pedersen Conductance in the Jovian Aurora

J.-C. Gérard¹ , L. Gkouvelis^{1,2} , B. Bonfond¹ , D. Grodent¹ , G. R. Gladstone^{2,3} , V. Hue³ , T. K. Greathouse³ , J. A. Kammer³ , M. Versteeg³ , and R. S. Giles³ 

¹LPAP, Université de Liège, Liège, Belgium, ²NASA/Ames Research Center, Mountain View, CA, USA, ³Space Science and Engineering, Southwest Research Institute, San Antonio, TX, USA

Abstract Ionospheric conductance contributes to regulate the characteristics of the ionospheric current and the closure of the magnetosphere-ionosphere circuit in the ionosphere. Measurements of Birkeland currents with the Juno magnetometer have indicated that they are statistically larger in the south. It has been suggested that these asymmetries may be the consequence of a higher Pedersen conductance in the southern hemisphere. We have derived the local precipitated electron energy flux and their characteristic energy from 14 multi-spectral images collected with the ultraviolet spectrograph on board Juno. This information was then used as input to an ionospheric model providing the density of H₃⁺, H⁺, and hydrocarbon ions to calculate the spatial distribution of the Pedersen conductance for Juno perijoves 1–15. We show that the area-integrated conductance is closely proportional to the H₃⁺ ion content and quasi equal in the north and the south. The mean conductance is 0.47 mho in both hemispheres. However, local variations in the Pedersen conductivity and/or hemispheric differences between the magnetospheric rotation and the rotation velocities of the neutrals can also result in asymmetry of Birkeland currents.

Plain Language Summary The electric conductance of Jupiter's partly controls the currents that circulate in its ionosphere and the current loops closing in this conducting region. Measurements of the ionospheric current intensity with the magnetometer along Juno's trajectory have shown that these currents are statistically stronger in the southern than in the northern hemisphere. A possibility has been raised that this asymmetry is related to a higher value of the Pedersen conductivity in the south. To test this hypothesis, we have compared the vertically integrated conductivity in both hemispheres derived from the intensity and spectral composition of images obtained with the Juno Ultraviolet Spectral Imager during its first 15 orbits around Jupiter. Comparison of the pairs of global conductance maps indicates that there is no significant statistical conductance asymmetry as both the area-integrated and the mean conductivity are quasi equal in the two hemispheres. Possible causes for the observed ionospheric current asymmetries are the local aspect of the magnetometer measurements and/or hemispheric differences between the magnetospheric rotation and the rotation velocities of the neutrals.

1. Introduction

The Pedersen conductivity characterizes the ability of ionospheres to carry currents perpendicular to the magnetic field in the presence of an electric field. On Jupiter, it is an important quantity that partly regulates how electric currents can circulate between the magnetosphere and the high-latitude ionosphere. It controls the flow of ionospheric current and the closure of the magnetosphere-ionosphere (M-I) circuit in the ionosphere. It is therefore a key element in the understanding of how and where the Jovian aurora is formed and how currents flow and heat up the neutral atmosphere. Model studies have investigated the magnitude and altitude distribution of Jupiter's ionospheric conductivity (Millward et al., 2002; Singhal, 1996; Strobel & Atreya, 1983). Nichols and Cowley (2004) showed that auroral precipitation can substantially modify the Pedersen vertically integrated conductivity (conductance) and influence the distribution and intensity of the field aligned currents closure in the auroral ionosphere. This interaction was subsequently introduced in 1-D, 2-D, and 3-D models (Bougher et al., 2005; Majeed et al., 2009; Ray et al., 2010, 2015; Smith & Aylward, 2009; Tao et al., 2009; Yates et al., 2012, 2020).

Numerical simulations by Millward et al. (2002) for different electron initial energies and precipitated energy fluxes showed that the main contribution to the auroral Pedersen conductance is from H_3^+ . These are the dominant ions over a wide range of altitudes in the auroral ionosphere. The density of H^+ becomes increasingly important relative to other ions at high altitude but its contribution to the integrated conductivity remains small in conditions of auroral precipitation. Gérard et al. (2020) used auroral spectral images collected with the ultraviolet spectrograph (UVS) on board the Juno spacecraft to calculate the spatial distribution of the conductivity profiles and create conductance maps. These results confirmed the leading role played by H_3^+ ions in the Pedersen conductance, but also pointed out the contribution of hydrocarbon ions formed near and below the homopause. They demonstrated that the Pedersen conductance is spatially highly variable with larger values generally located along the main auroral emission, the Io footprint and bright auroral polar spots.

Kotsiaros et al. (2019) analyzed azimuthal magnetic field perturbations detected with the Juno magnetometer when the spacecraft was crossing the auroral region. They derived the intensity of the downward current flowing into the ionosphere using Ampère's law and assuming azimuthal symmetry. They found that the total downward current varies significantly from ~ 6 to 62 MA in the north and ~ 26 to 91 MA in the south, with a mean value significantly larger (by a mean factor of ~ 2.4) in the southern hemisphere. To guarantee current conservation, the total downward current between the pole and Juno's footprint must be equal to the equatorward ionospheric Pedersen current. Kotsiaros et al. (2019) found that the mean ionospheric current density is $1.3 \mu A m^{-2}$ in the north and $3.1 \mu A m^{-2}$ in the south auroral region. They tentatively explained this difference by an asymmetry in the Pedersen conductance Σ_p . Since the Pedersen conductivity decreases with increasing B field intensity, they argued that this asymmetry may be caused by the weaker mean B-field intensity in the south allowing stronger currents to flow in the southern hemisphere. However, they pointed out that the azimuthal symmetry assumption could not be appropriate, as the Juno crossings could not be modeled by an infinite current sheet.

In this study, we take advantage of the capability of UVS on board Juno to determine the global distribution of the auroral conductance. We analyze global auroral images collected during the first 15 perijoves of the mission to assess the variability and detect possible Σ_p asymmetries. In particular, we address the following questions:

- How variable from orbit to orbit is the global hemispheric conductance?
- What is the main driver of this variability?
- Do the global conductance values derived from UVS spectral images indicate that the Pedersen conductance is globally larger in the south?

The method used to create auroral Pedersen conductance maps and quantify the hemispheric global conductance is explained in Section 2. Section 3.1 presents the results of the hemispheric area-integrated conductance, the mean conductance and the relationship between the H_3^+ ion hemispheric total content and the conductance. In Section 3.2, we create average north and south conductance maps and discuss their ratio. The absence of north-south conductance asymmetry and its relation to the current intensity is discussed in Section 4.

2. Methodology

The methodology we follow is largely based on the approach used by Gérard et al. (2020) to construct auroral Pedersen conductance maps based on observations made before and after Juno perijoves. In brief, we use the spacecraft rotation (30 s spin period) to construct multispectral images collected with the UVS instrument (Gladstone et al., 2017) on board the Juno spacecraft orbiting Jupiter (Bagenal et al., 2017; Bolton et al., 2017). A scan mirror allows UVS to move the field of view by up to 30° on either side of the spacecraft spin plane. The spectral resolution depends on which part of the "dog bone" entrance slit ($0.2^\circ \times 2.5^\circ$ or $0.025^\circ \times 2.0^\circ$) slit is used. The wide and narrow parts of the slit have a filled slit spectral resolution of 2.2 and 1.3 nm respectively (Greathouse et al., 2013). The point-spread function corresponds to about three detector pixels. The spatial resolution on the aurora is typically ~ 250 km perpendicular to the slit axis and 150 km along the slit at a distance of $1 R_J$ above the cloud top level. These spectral images are calibrated (Hue et al., 2019) and projected on orthographic maps from an altitude of 400 km above the 1 bar level

(Bonfond et al., 2015). The spatial resolution of the reconstructed maps is inversely proportional to the distance from the aurora and depends on the orientation of the slit relative to the arc or other auroral structure. It takes ~20 min and different scan mirror pointings to build a global image of the aurora in one hemisphere from a distance of 1.6 R_J .

The successive steps are as follows:

- the energy flux carried by the electrons is calculated on a latitude-longitude grid of $0.1^\circ \times 0.1^\circ$ on the basis of the unabsorbed H_2 auroral intensity between 155 and 162 nm (Bonfond et al., 2017). These values are multiplied by 8.1 to get the total H_2 emitted Lyman and Werner bands UV brightness. It is then assumed that 10 kR of H_2 emission are emitted for a precipitated electron flux F_e of 1 mW/m², as discussed by Gustin et al. (2016). The bins corresponding to the Io footprint and tail are manually excluded since they are spatially unrelated to the aurora and their structure and extension depends on the position of Io inside the plasma torus (Gérard et al., 2006)
- the FUV (CR) ratio of the two spectral bands $R = I(155\text{--}162\text{ nm})/I(126\text{--}130\text{ nm})$ is also calculated in each grid element. The 126–130 nm interval is used instead of the classical 123–130 nm to avoid contamination in the vicinity of the strong Lyman alpha hydrogen line at 121.6 nm also produced by electron impact on H_2 . The appropriate correction is applied based on a synthetic auroral spectrum (Gustin et al., 2013). R is related to the average electron energy

E_0 of the precipitating electrons. The relation derived by Gérard et al. (2002) and Gustin et al. (2016) is used to convert the color ratio into E_0 , based on the atmospheric model described by Grodent et al. (2001).

- the ionization rate profile $q(z)$ is calculated versus altitude using the auroral electron energy flux F_e and mean energy E_0 values for each bin from the analytical expressions given by Hiraki and Tao (2008)
- the $q(z)$ profiles are inputs to an ionosphere model describing the generation and loss of the different ion species (Gérard et al., 2020). The resulting vertical distributions of H_3^+ , hydrocarbon ions and electrons are then calculated for each UVS latitude-longitude bin
- the altitude-dependent Pedersen conductivity σ_p is obtained by adding the electron and ion contributions based on the classical Pedersen conductivity formulation combining the ion-neutral and the electron-neutral contributions:

$$\sigma_p^{\text{tot}} = \frac{eN_e}{B} \frac{\nu_{en}\omega_e}{\nu_{en}^2 + \omega_e^2} + \sum_i \frac{en_i}{B} \frac{\nu_{in}\omega_i}{\nu_{in}^2 + \omega_i^2}$$

where e is the electron charge, m_e the electron mass, ν_{en} the electron-neutral collision frequency, ω_e the electron gyration frequency, N_e the electron density, n_i is the density of ions i , ν_{in} is the ion-neutral collision frequency of ions i , ω_i their ion gyration frequency and B the magnetic field intensity. The contribution of the ions is dominant relative to the electrons. The Pedersen conductance Σ_p is the vertically integrated conductivity, expressed in mho. The magnetic field intensity is provided by the JRM09 model, based on magnetometer measurements on board Juno (Connerney et al., 2018).

- The conductivity σ_p is integrated with respect to altitude to obtain a two dimensional map of the auroral Pedersen conductance Σ_p

Eight examples of Pedersen conductance and H_3^+ column density maps have been illustrated in Gérard et al. (2020). They demonstrated the nonuniformity of the auroral conductance, showing local values ranging from less than 0.1 to several mhos. The largest values were obtained in the main UV emission, the Io auroral footprint and in the bright spot regions frequently observed at high latitude. In their preliminary study, the conductance values appeared to show limited variability between orbits, but maps in both hemispheres were only obtained for Juno's orbit 12.

For this study, 14 auroral conductance maps were constructed for both hemispheres, corresponding to peri-joves (PJs) 1–15, with the exception of orbit 2 when the scientific instruments were not operating. We first analyze global conductances by integrating the individual conductance maps over the auroral area in each hemisphere separately. We examine the variability of these area-integrated conductance maps. We then determine their north to south ratio and the mean hemispheric conductance values. In a second approach,

Table 1
Observed Hemispheric Emitted H_2 Auroral Power (10^{12} W), Correction Factor for Missing Data and Corrected Emitted Power

Perijove	N/S	Observed power (TW)	Area ratio	Corrected power (TW)
PJ1	N	2.82	1.00	2.82
PJ1	S	2.46	0.97	2.54
PJ3	N	1.26	0.99	1.27
PJ3	S	1.82	1.00	1.82
PJ4	N	1.05	0.85	1.24
PJ4	S	1.41	1.00	1.41
PJ5	N	2.32	0.96	2.42
PJ5	S	1.84	0.99	1.85
PJ6	N	1.98	0.99	1.99
PJ6	S	1.74	0.95	1.83
PJ7	N	2.12	1.00	2.12
PJ7	S	1.92	0.99	1.92
PJ8	N	1.48	0.99	1.48
PJ8	S	1.52	0.97	1.57
PJ9	N	1.80	0.98	1.84
PJ9	S	2.24	1.00	2.24
PJ10	N	2.17	0.85	2.54
PJ10	S	3.23	1.00	3.24
PJ11	N	2.38	0.96	2.48
PJ11	S	1.26	1.00	1.26
PJ12	N	1.88	1.00	1.88
PJ12	S	2.08	0.99	2.10
PJ13	N	1.26	1.00	1.26
PJ13	S	1.09	1.00	1.09
PJ14	N	1.21	0.92	1.31
PJ14	S	1.27	0.98	1.29
PJ15	N	2.29	0.93	2.48
PJ15	S	3.16	0.99	3.20

Note. Mean corrected north power and standard deviation of the mean. North: $\mu = 1.94$ TW, $\sigma_\mu = 0.14$ TW; South: $\mu = 1.95$ TW, $\sigma_\mu = 0.17$ TW. N/S ratio of the mean = 0.99.

we create average north and south conductance maps from the 28 individual maps and calculate the ratio of their area-integrated Pedersen conductance.

3. Results

3.1. Hemispheric Conductance, Variability and Symmetry

The area (in km^2) subtended by each bin is calculated from their projection on Jupiter. These areas depend on the Juno-Jupiter distance and the emission angle. They are used to calculate the hemispheric area-integrated conductance from the expression:

$$\Sigma_p(HI) = \int_S \Sigma_p dS$$

where the integral includes all auroral map elements with the exception of the Io footprint and tail.

During the period between PJ1 and PJ15, the spacecraft orbital precession brought Juno deeper into the radiation belts and the visibility of the northern aurora slightly deteriorated. These changes caused the appearance of regions void of observation. To mitigate these effects, we have corrected for the missing data of each perijove by dividing the observed power by the fractional auroral area actually covered in each image. An estimate of the associated uncertainty is obtained by comparing the values corrected following this procedure with cases PJ1 north and PJ3 south with full coverage (Table 1). We estimate the corresponding uncertainty as less than 2% for the south cases, between 1% and 3% in the north except for PJ4 and PJ15 (11%) and PJ4 (7%). The $\Sigma_p(HI)$ values for each perijove are presented in Table 2 and plotted in Figure 1a. They vary by less than a factor of two in both hemispheres, ranging from 5.6×10^8 to 9.3×10^8 mho km^2 in the north and 4.9×10^8 mho km^2 to 8.8×10^8 in the south. The N/S ratio is highest for PJ6 (1.5) and lowest for PJ8 and PJ10 (0.8). The mean N/S ratio is 1.1 with a 1- σ standard error of 0.06. One notes that PJ1 shows the highest integrated conductance in both hemispheres. These orbit-to-orbit variations are much less than the changes of the ionospheric currents measured by the Juno magnetometer in the northern auroral region by Kotsiaros et al. (2019). The relative intensity and morphological characteristics of the aurora observed in both hemispheres during PJ1 were discussed by Bonfond et al. (2017). No trend in the time variation or significant north-south correlation is observed in Figure 1a.

The evolution of the area-integrated H_3^+ column density, that is the dimensionless total number of H_3^+ ionospheric ions in one hemisphere, is also shown in Figure 1. This plot shows similarity with panel (a) for

both hemispheres, suggesting a causal relationship between the two quantities. This correlation is further demonstrated in Figure 2 where the variation of the Pedersen conductance is shown versus the corresponding H_3^+ hemispheric content. In this plot only latitude-longitude bins filled with data have been considered. A correlation is observed in Figure 2 for both northern and southern hemispheres. The linear correlation coefficients are 0.91 for the north and 0.98 for the south. The values in the north for given levels of H_3^+ content are similar to or slightly larger than in the south. These results are in agreement with one-dimensional models of auroral Pedersen conductance (Hiraki & Tao, 2008; Millward et al., 2002) that have shown that the amount of H_3^+ ions is the key quantity controlling the Pedersen conductance. In turn, the H_3^+ content in each hemisphere varies nearly proportionally to the square root of the precipitated auroral power (Gérard et al., 2020; Tao et al., 2011).

Table 2
Area-Integrated Pedersen Conductance and Their Hemispheric Ratio
(Corrected for Missing Data)

PJ	North (10^8 mho km^2)	South (10^8 mho km^2)	Σ_p N/S ratio
1	9.3	8.8	1.1
3	6.2	6.7	0.9
4	6.0	6.8	0.9
5	7.7	6.4	1.2
6	7.1	4.9	1.5
7	7.1	6.1	1.2
8	6.8	8.2	0.8
9	7.1	6.2	1.1
10	6.4	7.6	0.8
11	7.0	5.3	1.3
12	6.0	4.4	1.4
13	5.6	5.7	1.0
14	6.7	6.5	1.0
15	7.2	7.6	1.0

The values of the mean hemispheric conductance have also been calculated for each of the 14 spectral images using the expression:

$$\overline{\Sigma_p} = \frac{\int_S \Sigma_p dS}{\int_S dS}$$

The values of Σ_p are listed in Table 3 and their evolution is plotted in Figure 3. The mean hemispheric conductances Σ_p vary from 0.46 to 0.66 mho in the north and 0.48 to 0.74 mho in the south, with mean values of 0.50 and 0.53 mho respectively. The N/S ratio of the hemispheric mean conductances varies from 0.71 to 1.39. Although their ratio shows limited variations, the mean conductances are better correlated between the two hemispheres than the area integrated values shown in Figure 1a.

The variations of the north/south ratio of the area-integrated conductance are listed in the last column of Table 2. They are represented in Figure 4 by the red dots, together with the total H_3^+ content. The two quantities clearly co-vary as expected from the dominant role of H_3^+ ions in the value of the Pedersen conductance.

3.2. Mean Hemispheric Conductance Maps and Their Ratio

Another approach to quantify the mean ratio of the Pedersen auroral conductance is to first create mean conductance maps in both hemispheres, calculate the integrated conductance value and examine their ratio. The mean conductance maps are obtained by co-adding the values of Σ_p in each latitude-longitude and dividing this sum by the number of contributions inside each bin. The resulting maps are shown in Figure 5. As before, the contribution of the Io footprints and trailing tails have been removed. A statistical region of conductance less than 0.2 mho is seen slightly shifted from the south pole along the 30° S_{III} meridian. In the north, a minimum is located near 70° N and a S_{III} longitude of 185° . The highest values are roughly co-located with the position of the H_2 statistical main emission (Bonfond et al., 2012; Grodent et al., 2003). This near-coincidence is consistent with the idea that the electron energy flux is the main driver for both the H_2 auroral intensity and the production of H_3^+ ions, which in turn mostly control the value of the Pedersen conductance.

The integrated Pedersen conductance is 1.24×10^9 mhos km^2 in the north and 1.23×10^9 mhos km^2 in the south, leading to a north/south ratio of 1.006, implying that it is not statistically different from 1. The mean conductance value in the northern hemisphere is 0.470 mho, also very close to 0.465 mho in the south, corresponding to a hemispheric ratio of 1.01, not significantly different from unity.

Our conductance maps show values in the range 0.3–1.2 mho along the main ultraviolet emission. These values are comparable to those obtained in numerical simulations with models of M-I coupling. Examples of peak values in the modeled latitudinal distribution include 0.25 mho in the JIM model (Millward et al., 2002), 0.75 mho (Tao et al., 2009), 0.7 mho (Ray et al., 2015), but up to 12 mhos in Bougher et al.'s JTGCM (2005).

4. Discussion

These results lead to the conclusion that the global hemispheric conductance varies by less than a factor of 2 between for the data collected during the 14 individual Juno perijove passes. This is a consequence of the relatively limited changes observed in the global auroral intensity,

calculate the integrated conductance value and examine their ratio. The mean conductance maps are obtained by co-adding the values of Σ_p in each latitude-longitude and dividing this sum by the number of contributions inside each bin. The resulting maps are shown in Figure 5. As before, the contribution of the Io footprints and trailing tails have been removed. A statistical region of conductance less than 0.2 mho is seen slightly shifted from the south pole along the 30° S_{III} meridian. In the north, a minimum is located near 70° N and a S_{III} longitude of 185° . The highest values are roughly co-located with the position of the H_2 statistical main emission (Bonfond et al., 2012; Grodent et al., 2003). This near-coincidence is consistent with the idea that the electron energy flux is the main driver for both the H_2 auroral intensity and the production of H_3^+ ions, which in turn mostly control the value of the Pedersen conductance.

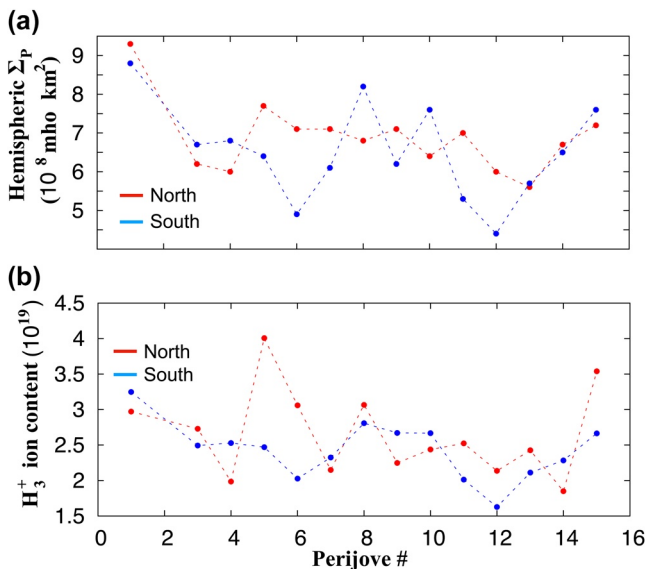


Figure 1. (a) Area-integrated conductance in the northern (red dots) and southern (blue dots) hemispheres for Juno perijove passes 1–15 expressed in mho km^2 (b) total dimensionless number of H_3^+ ions in both hemispheres.

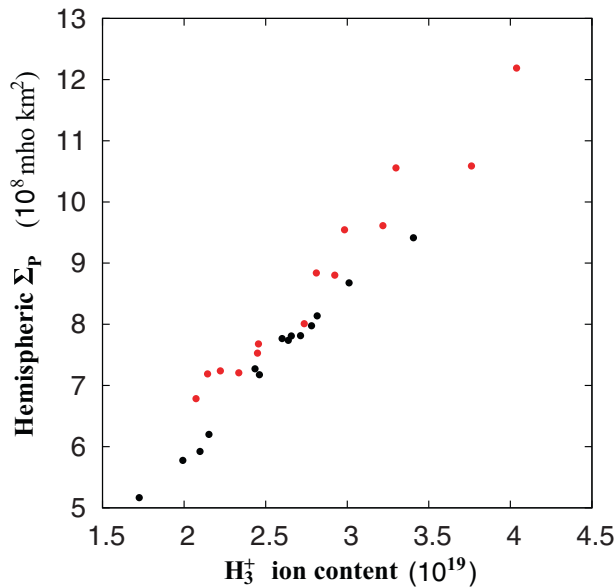


Figure 2. Correlation between the hemispheric auroral conductance and the total number of H_3^+ ions in the northern (red dots) and southern (black dots) auroral hemispheres.

ences in the brightness and integrated conductance may stem from the time delay between the images in the north and in the south. As mentioned earlier, the H_2 power is closely proportional to the power carried by the auroral electron flux. The mean value of the N/S ratio of emitted hemispheric power is 1.04 following correction for coverage gaps (Table 4), and 0.94 in the noncorrected case, also in statistical agreement with a nearly equal power emitted in the two hemispheres.

No evidence is thus observed for a statistically significant difference between the Pedersen conductances of the two hemispheres nor between the precipitated power carried by the energetic auroral particles. This

result may appear counter-intuitive if the magnetic field intensity was globally stronger in the north than in the south. Our numerical simulations have indeed confirmed that the Pedersen conductance decreases with increasing values of the magnetic field value. However, it is important to note that the north B-field is only stronger than the south in a limited segment (140° – 220°) of the north statistical auroral oval (Connerney et al., 2018; Gérard et al., 2013) and weaker elsewhere. In any case, our analysis of the hemispheric UVS auroral images leads to the conclusion that we do not observe statistically significant difference in the auroral emitted power or, if any, to a slightly larger value in the north.

The total H_2 emitted power corrected for the missing data is found to vary by a factor of about 2.8 with values between 1.09 and 3.24 TW with a mean value of 1.94 in the north and 1.95 TW in the south (Table 1), in good agreement with those derived from Hubble auroral images by Grodent et al. (2018) showing values between 1 and 3 TW. Part of the hemispheric differ-

ences in the brightness and integrated conductance may stem from the time delay between the images in the north and in the south. As mentioned earlier, the H_2 power is closely proportional to the power carried by the auroral electron flux. The mean value of the N/S ratio of emitted hemispheric power is 1.04 following correction for coverage gaps (Table 4), and 0.94 in the noncorrected case, also in statistical agreement with a nearly equal power emitted in the two hemispheres.

The spatial variability of the vertical and horizontal methane distribution in the Jovian upper atmosphere is still largely unexplored. Missing observational information on this question, we have assumed that the vertical CH_4 distribution is spatially uniform in the auroral region. Recent ground-based infrared spectral observations by Sinclair et al. (2020) suggest that the altitude of the hydrocarbon homopause may increase inside the aurora relative to lower latitude regions. They claim that the homopause altitude in the north is higher by about 100 km in the aurora than outside. However, these observations did not allow detailed mapping the altitude of the homopause. There is also a possibility that the altitude of the methane homopause is different between the two hemispheres and spatially variable inside the different auroral regions (main oval, active

Table 3
Mean Hemispheric Conductance (mho)

Perijove	North	South
1	0.66	0.74
3	0.47	0.53
4	0.48	0.47
5	0.49	0.49
6	0.47	0.55
7	0.59	0.59
8	0.48	0.50
9	0.47	0.55
10	0.49	0.54
11	0.48	0.51
12	0.46	0.48
13	0.51	0.51
14	0.54	0.53
15	0.55	0.58

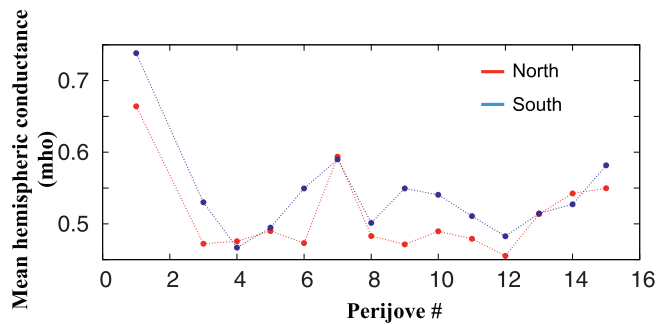


Figure 3. Mean hemispheric conductance in the northern (red dots) and southern hemispheres (blue dots) (see text).

and swirl regions, and equatorward aurora). However, the existence and the amplitude of these variations are essentially unknown at this point. If the homopause altitude varies from region to region, it would modify the CR- E_0 relation in a way depending on the local strength of the hydrocarbon upwelling and effect the calculated penetration depth of the electrons. As a sensitivity test, we have modified the CR- E_0 relationship. For example, an increase of the eddy diffusion coefficient at the homopause from 1.4×10^6 to 1.4×10^7 $\text{cm}^2 \text{s}^{-1}$ in the Grodent et al.'s 1-D model corresponds to an upward shift of the methane homopause of 66 km. The modified CR- E_0 relation between the mean electron energy and the color ratio has been applied to UVS data images from perijove 1. The results show that the area-integrated conductance increases by a factor of 1.16. The N/S ratio of the integrated Σ_p remains equal to 1.1, as in the standard case. The N/S ratio of the mean global conductivity is 0.95 (compared to 0.90). Therefore, even if the global conductance shows some dependence

on the CR- E_0 relationship, the ratio of the hemispheric conductance values remains quasi constant and equal in the two hemispheres.

The global conductance symmetry is in contrast, but not necessarily in contradiction, with the measurements by Kotsiaros et al. (2019) indicating that the ionospheric currents are stronger in the southern auroral region. However, we do not confirm the assumption that this asymmetry results from differences in the Pedersen conductances, at least not on a global scale. One aspect is that the measured ionospheric current asymmetries are local, but are not global in the hemisphere and do not satisfy the assumption of azimuthal symmetry of the currents. Our results do not necessarily overrule local conductance asymmetries averaged along the ionospheric projection of the Juno trajectories that only sample a limited fraction of the auroral ionosphere. Future studies with more extended coverage may establish whether the current asymmetry is global.

Another possible explanation is that, despite the intrinsic Pedersen conductance symmetry, the intensity of the current flow is not symmetrical. Two force balances must be considered: (1) the balance between the Lorentz force (depends on $\mathbf{j} \times \mathbf{B}$) and the neutral-ion collision force on the ionospheric ions (that depends on the momentum cross section and the relative velocities of ions and neutrals) and (2) the balance between the ion-neutral collision force and a combination of vertical propagated viscosity (that depends on the eddy diffusion profile) and the horizontal wind system. This suggests that the high-latitude eddy diffusion coefficient and the wind system asymmetries are important factors that drive the observed auroral current symmetry. In particular, the existence of polar vortices suggests that the vertically propagated viscous momentum from the lower atmosphere is not a simple corotational flow and the overlay of the Pedersen conductivity enhancements onto the polar vortex grids are very different between the south and the north.

Majeed et al. (2016)'s model simulations resulted in a plasma drift about 20% stronger in the southern than in the northern polar region as a consequence of the value of the mapping of the VIP4 magnetic field.

Consequently, a larger departure of the southern polar drifts from corotation than in the north was predicted. Huang and Hill (1989) found that the neutral atmosphere at ionospheric heights must "slip" relative to the deeper atmosphere. In this view, the altitude variation of the drift velocities of neutrals and ions in the ionosphere and the corotation lag of the magnetosphere are related to the atmospheric eddy diffusion coefficient at ionospheric heights. They assumed that this slippage could be parameterized in terms of an effective ionospheric Pedersen conductance convenient for use in M-I coupling models. The Pedersen conductance calculations in this study do not include this effect. M-I coupling models accounting for this effect have been described by Huang and Hill (1989), Smith and Aylward (2009), Ray et al. (2015), and Yates et al. (2020). An effective Pedersen conductance has been defined, equal to the intrinsic conductance multiplied by a correction factor (1-K), where K is the proportion of the co-rotation lag.

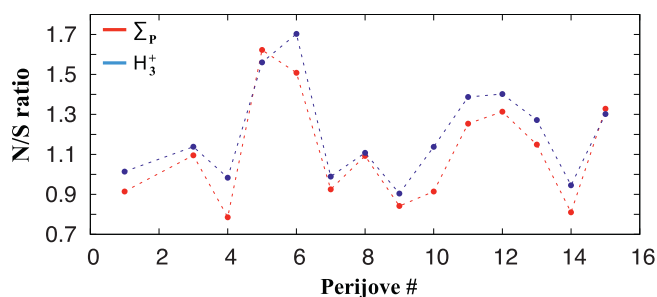


Figure 4. North/south ratio of the area-integrated conductance (red dots) and the H_3^+ ion content (blue dots).

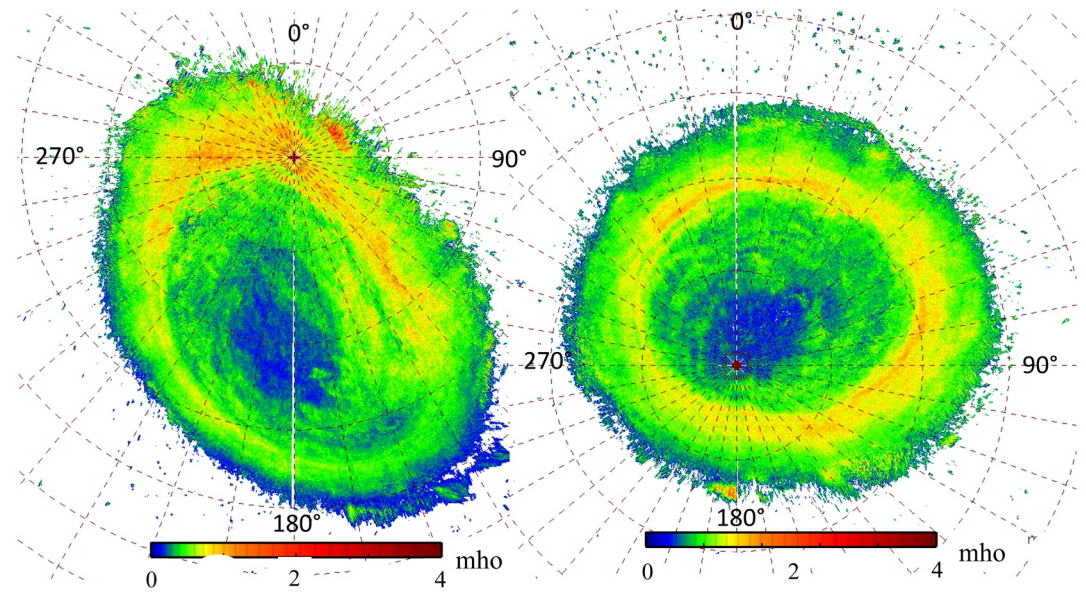


Figure 5. Average Pedersen conductance maps for the northern (left) and southern (right) hemispheres based on 14 Juno perijoves. The southern hemisphere is represented as if observed through the planet. System III longitudes are indicated every 90°.

5. Conclusions

The results reported in this study lead to several interesting conclusions concerning the variability and hemispheric symmetry of Pedersen conductance in the Jovian aurora.

We have built and compared 28 Pedersen conductance maps based on Juno-UVS spectral images from the first 15 perijoves and an auroral ionospheric model. We find that the orbit-to-orbit variability of the hemispheric auroral Pedersen conductance is less than a factor of 2, although its spatial distribution may be quite variable. The area-integrated hemispheric conductance varies quasi-proportionally to the integrated H_3^+ ion content.

Statistically, both methods described in Section 3 lead to the conclusion that there is no indication that the Pedersen conductance is significantly larger in the southern hemispheres than in the north, although it may be the case in some sectors. This conclusion is based on the mean value of 1.04 of the ratio of the conductances associated with each perijove and on the equality of the hemispheric values of mean conductance maps constructed from the 14 Juno orbits. We have also derived the auroral emitted power carried by the precipitated electron and found that it varied by a factor of about 2.9, with values ranging from 1.1 to 3.2 TW. On the average, the emitted power is equal in the two hemispheres within 4%.

We conclude that the asymmetry of the field-aligned currents measured with the magnetometer on board Juno does not appear to be caused by hemispheric differences in the magnitude of the area-integrated auroral nor the hemispheric average of the Pedersen conductance. However, we cannot reject the possibility that the asymmetry could be due to variations in the local Pedersen conductivity nor the hemispheric differences in the amount of ionospheric slippage and atmospheric conditions.

Table 4
North/South Ratio of the H_2 Emitted Auroral Power Without and With Correction for Missing Data

Perijove	Uncorrected	Corrected
PJ1	1.15	1.11
PJ3	0.69	0.70
PJ4	0.74	0.88
PJ5	1.26	1.30
PJ6	1.14	1.09
PJ7	1.10	1.10
PJ8	0.97	0.94
PJ9	0.80	0.82
PJ10	0.67	0.78
PJ11	0.89	1.95
PJ12	0.91	0.90
PJ13	1.16	1.16
PJ14	0.95	1.02
PJ15	0.72	0.78

Note. Mean ratio (noncorrected) and standard error of the mean: $\mu = 0.94$, $\sigma_\mu = 0.05$. Mean ratio (corrected) and standard error of the mean: $\mu = 1.04$, $\sigma_\mu = 0.08$.

Data Availability Statement

The data included herein are either archived or on schedule to be archived in NASA's Planetary Data System (PDS) (http://pds-atmospheres.nmsu.edu/data_and_services/atmospheres_data/JUNO/juno.html).

Acknowledgments

L. Gkouvelis was supported for this research by an appointment to the National Aeronautics and Space Administration (NASA) Postdoctoral Program at the Ames Research Center administrated by the Universities Space Research Association (USRA) through a contract with NASA. B. Bonfond is a Research Associate of the Belgian Fonds de la Recherche Scientifique-FNRS. J.-C. Gérard, B. Bonfond, and D. Grodent acknowledge financial support from the Belgian Federal Science Policy Office (BELSPO) via the PRODEX Program of ESA. We are grateful to NASA and contributing institutions that have made the Juno mission possible. This work was funded by NASA's New Frontiers Program for Juno via contract with the Southwest Research Institute.

References

- Bagenal, F., Adriani, A., Allegrini, F., Bolton, S. J., Bonfond, B., Bunce, E. J., et al. (2017). Magnetospheric science objectives of the Juno mission. *Space Science Reviews*, *213*(1–4), 219–287.
- Bolton, S. J., Lunine, J., Stevenson, D., Connerney, J. E. P., Levin, S., Owen, T. C., et al. (2017). The Juno mission. *Space Science Reviews*, *213*(1–4), 5–37.
- Bonfond, B., Gladstone, G. R., Grodent, D., Greathouse, T. K., Versteeg, M. H., Hue, V., et al. (2017). Morphology of the UV aurorae Jupiter during Juno's first perijove observations. *Geophysical Research Letters*, *44*(10), 4463–4471. <https://doi.org/10.1002/2017GL073114>
- Bonfond, B., Grodent, D., Gérard, J. C., Stallard, T., Clarke, J. T., Yoneda, M., et al. (2012). Auroral evidence of Io's control over the magnetosphere of Jupiter. *Geophysical Research Letters*, *39*, L01105. <https://doi.org/10.1029/2011GL050253>
- Bonfond, B., Gustin, J., Gérard, J. C., Grodent, D., Radioti, A., Palmaerts, B., et al. (2015). The far-ultraviolet main auroral emission at Jupiter—Part 2: Vertical emission profile. *Annals of Geophysics*, *33*, 1211–1219.
- Bougher, S. W., Waite, J. H., Jr, Majeed, T., & Gladstone, G. R. (2005). Jupiter Thermospheric General Circulation Model (JTGCM): Global structure and dynamics driven by auroral and Joule heating. *Journal of Geophysical Research*, *110*, E04008. <https://doi.org/10.1029/2003JE002230>
- Clarke, J. T., Nichols, J., Gérard, J. C., Grodent, D., Hansen, K. C., Kurth, W., et al. (2009). Response of Jupiter's and Saturn's auroral activity to the solar wind. *Journal of Geophysical Research*, *114*, A05210. <https://doi.org/10.1029/2008JA013694>
- Connerney, J. E. P., Kotsiaros, S., Oliverson, R. J., Espley, J. R., Jørgensen, J. L., Joergensen, P. S., & Bolton, S. J. (2018). A new model of Jupiter's magnetic field from Juno's first nine orbits. *Geophysical Research Letters*, *45*, 2590–2596. <https://doi.org/10.1002/2018GL077312>
- Gérard, J. C., Gkouvelis, L., Bonfond, B., Grodent, D., Gladstone, G. R., Hue, V., et al. (2020). Spatial distribution of the Pedersen conductance in the Jovian Aurora from Juno-UVS spectral images. *Journal of Geophysical Research: Space Physics*, *125*(8). e2020JA028142. <https://doi.org/10.1029/2020JA028142>
- Gérard, J. C., Grodent, D., Radioti, A., Bonfond, B., & Clarke, J. T. (2013). Hubble observations of Jupiter's north–south conjugate ultraviolet aurora. *Icarus*, *226*, 1559–1567.
- Gérard, J. C., Gustin, J., Grodent, D., Delamere, P., & Clarke, J. T. (2002). The excitation of the FUV Io tail on Jupiter: Characterization of the electron precipitation. *Journal of Geophysical Research*, *107*(A11), 1394. <https://doi.org/10.1029/2002JA009410>
- Gérard, J. C., Saglam, A., Grodent, D., & Clarke, J. T. (2006). Morphology of the ultraviolet Io footprint emission and its control by Io's location. *Journal of Geophysical Research*, *111*, A04202. <https://doi.org/10.1029/2005JA011327>
- Gladstone, G. R., Persyn, S. C., Eterno, J. S., Walther, B. C., Slater, D. C., Davis, M. W., & Sawka, A. O. (2017). The ultraviolet spectrograph on NASA's Juno mission. *Space Science Reviews*, *213*(1–4), 447–473.
- Greathouse, T. K., Gladstone, G. R., Davis, M. W., Slater, D. C., Versteeg, M. H., Persson, K. B., et al. (2013). Performance results from in-flight commissioning of the Juno ultraviolet spectrograph (Juno-UVS). In *Proceedings UV, X-Ray, and Gamma-Ray Space Instrumentation for Astronomy XVIII*. (Vol. 8859, p. 88590T). International Society for Optics and Photonics.
- Grodent, D., Bonfond, B., Yao, Z., Gérard, J. C., Radioti, A., Dumont, M., et al. (2018). Jupiter's aurora observed with HST during Juno orbits 3 to 7. *Journal of Geophysical Research: Space Physics*, *123*, 3299–3319. <https://doi.org/10.1002/2017JA025046>
- Grodent, D., Clarke, J. T., Kim, J., Waite, J. H., & Cowley, S. W. H. (2003). Jupiter's main auroral oval observed with HST-STIS. *Journal of Geophysical Research*, *108*(A11), 1389. <https://doi.org/10.1029/2003JA009921>
- Grodent, D., Waite, J. H., Jr, & Gérard, J. C. (2001). A self-consistent model of the Jovian auroral thermal structure. *Journal of Geophysical Research*, *106*(A7), 12933–12952.
- Gustin, J., Gérard, J. C., Grodent, D., Gladstone, G. R., Clarke, J. T., Pryor, W. R., et al. (2013). Effects of methane on giant planet's UV emissions and implications for the auroral characteristics. *Journal of Molecular Spectroscopy*, *291*, 108–117.
- Gustin, J., Grodent, D., Ray, L. C., Bonfond, B., Bunce, E. J., Nichols, J. D., & Ozak, N. (2016). Characteristics of north Jovian aurora from STIS FUV spectral images. *Icarus*, *268*, 215–241.
- Hiraki, Y., & Tao, C. (2008). Parameterization of ionization rate by auroral electron precipitation in Jupiter. *Annals of Geophysics*, *26*, 77–86.
- Huang, T. S., & Hill, T. W. (1989). Corotation lag of the Jovian atmosphere, ionosphere, and magnetosphere. *Journal of Geophysical Research*, *94*(A4), 3761–3765. <https://doi.org/10.1029/JA094iA04p03761>
- Hue, V., Gladstone, G. R., Greathouse, T. K., Kammer, J. A., Davis, M. W., Bonfond, B., et al. (2019). In-flight characterization and calibration of the Juno Ultraviolet Spectrograph (Juno-UVS). *The Astronomical Journal*, *157*, 90. <https://doi.org/10.3847/1538-3881/aafb36>
- Kotsiaros, S., Connerney, J. E., Clark, G., Allegrini, F., Gladstone, G. R., Kurth, W. S., & Martos, Y. M. (2019). Birkeland currents in Jupiter's magnetosphere observed by the polar-orbiting Juno spacecraft. *Nature Astronomy*, *3*(10), 904–909.
- Majeed, T., Bougher, S. W., Ridley, A. J., Waite, J. H., Gladstone, G. R., & Bell, J. M. (2016). Global response of the upper thermospheric winds to large ion drifts in the Jovian ovals. *Journal of Geophysical Research: Space Physics*, *121*, 4647–4667. <https://doi.org/10.1002/2015JA021328>
- Majeed, T., Waite, J. H., Bougher, S. W., & Gladstone, G. R. (2009). Processes of auroral thermal structure at Jupiter: Analysis of multispectral temperature observations with the JTGCM. *Journal of Geophysical Research*, *114*, E07005. <https://doi.org/10.1029/2008JE003194>
- Millward, G., Miller, S., Stallard, T., Aylward, A. D., & Achilleos, N. (2002). On the dynamics of the Jovian ionosphere and thermosphere: III. The modelling of auroral conductivity. *Icarus*, *160*, 95–107.
- Nichols, J., Clarke, J. T., Gérard, J. C., Grodent, D., & Hansen, K. C. (2009). Variation of different components of Jupiter's auroral emission. *Journal of Geophysical Research*, *114*, 6210. <https://doi.org/10.1029/2009JA014051>
- Nichols, J., & Cowley, S. (2004). Magnetosphere-ionosphere coupling currents in Jupiter's middle magnetosphere: Effect of precipitation-induced enhancement of the ionospheric Pedersen conductivity. *Annals of Geophysics*, *22*, 1799–1827. <https://doi.org/10.5194/angeo-22-1799-2004>
- Ray, L. C., Achilleos, N. A., & Yates, J. N. (2015). The effect of including field-aligned potentials in the coupling between Jupiter's thermosphere, ionosphere, and magnetosphere. *Journal of Geophysical Research: Space Physics*, *120*, 6987–7005. <https://doi.org/10.1002/2015JA021319>

- Ray, L. C., Ergun, R. E., Delamere, P. A., & Bagenal, F. (2010). Magnetosphere-ionosphere coupling at Jupiter: Effect of field-aligned potentials on angular momentum transport. *Journal of Geophysical Research*, *115*(A9). <https://doi.org/10.1029/2010JA015423>
- Sinclair, J. A., Greathouse, T. K., Giles, R. S., Antuñano, A., Moses, J. I., Fouchet, T., et al. (2020). Spatial variations in the Altitude of the CH₄ homopause at Jupiter's mid-to-high latitudes, as constrained from IRTF-TEXES spectra. *The Planetary Science Journal*, *1*(3), 85. <https://doi.org/10.3847/PSJ/abc887>
- Singhal, R. P. (1996). Hall and Pedersen conductivities in the auroral ionosphere of Jupiter. *Indian Journal of Radio and Space Physics*, *25*(6), 361–366.
- Smith, C. G. A., & Aylward, A. D. (2009). Coupled rotational dynamics of Jupiter's thermosphere and magnetosphere. *Annales Geophysicae*, *27*, 199–230.
- Strobel, D. F., & Atreya, S. K. (1983). Ionosphere. In A. Dessler (Ed.), (Ed), *Physics of the Jovian Magnetosphere* (pp. 51–67). England: Cambridge University Press.
- Tao, C., Badman, S. V., & Fujimoto, M. (2011). UV and IR auroral emission model for the outer planets: Jupiter and Saturn comparison. *Icarus*, *213*(2), 581–592.
- Tao, C., Fujiwara, H., & Kasaba, K. (2009). Neutral wind control of the Jovian magnetosphere-ionosphere current system. *Journal of Geophysical Research*, *114*, A08307. <https://doi.org/10.1029/2008JA013966>
- Yates, J. N., Achilleos, N., & Guio, P. (2012). Influence of upstream solar wind on thermospheric flows at Jupiter. *Planetary and Space Science*, *61*(1), 15–31.
- Yates, J. N., Ray, L. C., Achilleos, N., Witasse, O., & Altobelli, N. (2020). Magnetosphere-Ionosphere-Thermosphere coupling at Jupiter using a three-dimensional atmospheric general circulation model. *Journal of Geophysical Research: Space Physics*, *125*. e2019JA026792. <https://doi.org/10.1029/2019JA026792>